Mat Res Innovat (2000) 3:190–204

ORIGINAL ARTICLE

A. Meldrum · L.A. Boatner · C.W. White
R.C. Ewing

Ion irradiation effects in nonmetals: formation of nanocrystals and novel microstructures

Received: 28 October 1999 / Reviewed and accepted: 12 November 1999

Abstract Ion implantation is a versatile and powerful technique for producing nanocrystal precipitates embedded in the near-surface region of materials. Radiation effects that occur during the implantation process can lead to complex microstructures and particle size distributions, and in the present work, we focus on the application of these effects to produce novel microstructural properties for insulating or semiconducting nanocrystals formed in optical host materials. Nanocrystal precipitates can be produced in two ways: by irradiation of pure (*i.e.*, non-implanted) crystalline or amorphous materials, or by ion implantation followed by either thermal annealing or subsequent additional irradiation. Different methods for the formation of novel structural relationships between embedded nanocrystals and their hosts have been developed, and the results presented here demonstrate the general flexibility of ion implantation and irradiation techniques for producing unique near-surface nanocomposite microstructures in irradiated host materials.

Key words Zircon · Pretulite · Nanocrystals · Irradiation · Semiconductors · Microstructure · Nonmetals · ZnS · CdS

Introduction

The use of nanocrystalline materials based on their optical properties can be traced back to at least 1685 when Andreas Cassius produced a glass with an unusual color called "the purple of Cassius", subsequently to become known as "gold-ruby" glass. This example of colored glass was created by adding small quantities of gold to the glass frit during melting, followed by a careful annealing process. In 1857, Michael Faraday correctly attributed the characteristic red color of gold ruby glass to the presence of finely dispersed nanocrystalline particles of gold [1]. In 1908, Gustav Mie developed the theoretical explanation of the process by which light is scattered from small particles [2] giving rise to the characteristic color of gold-ruby glass and of other glasses containing nanophase precipitates.

More recently, new and useful optical and electronic effects associated with metal, semiconductor, and oxide nanocrystals have been discovered. For example, high concentrations of metal nanoparticles in a transparent host can be used to obtain large third-order optical nonlinearities with potential applications in integrated optical devices. Semiconductor nanocrystals have been found to exhibit a number of size-dependent opto-electronic effects. Specifically, the energy of the bandgap can be modified in sufficiently small particles due to the quantum confinement of excitons. These modifications can lead to relatively large blueshifts in the absorption and photoluminescence spectra. Semiconductor nanocrystals are, in fact, already beginning to find applications as dyes and optical sensors [3, 4].

Ion implantation is a technique that has recently attracted a high level of interest as a versatile method of forming a wide variety of nanocrystal compositions in effectively any host material. In the particular case of metallic nanoparticles, ion implantation offers the advantage that a much higher local concentration of nanocrystal precipitates can be achieved than those produced, for example, in bulk glass by more traditional approaches, leading to enhanced third-order optical nonlinearity effects. On the other hand, ion implantation, by its very nature, produces significant radiation effects in the host material. These effects can lead to unusual microstructures or large size dispersions of embedded nanocrystal precipitates. While these effects are often considered to be undesirable, particularly if the nanoparticle-induced

A. Meldrum (✉)
The University of Alberta, Dept. of Physics, Edmonton, AB, Canada T6G 2J1
e-mail: dept@phys.ualberta.ca

L.A. Boatner · C.W. White
Oak Ridge National Laboratory, Solid State Division, Oak Ridge, TN 37831-6056, USA

R.C. Ewing
The University of Michigan, Dept. of NE&RS, Ann Arbor, MI 48109-2104, USA

optical effects depend on the size or microstructure of the precipitates, the unusual or unexpected microstructures that form as a result of irradiation may actually be exploited and find use in future generations of optical devices.

The present work is directed toward investigations of the effects of irradiation on the formation of nanocrystal precipitates, and on the unique microstructures that can be formed by this approach. The objective of this work is approached in two ways: First, we examine various phases that could potentially to be used for the formation of nanocrystals by direct ion irradiation – that is, without any significant change in the local chemistry of the system due to the introduction of the implanted ions. In this regard, both zircon ($ZrSiO_4$) and its isostructural phosphate analogue pretulite ($ScPO_4$) were investigated. Zircon has been shown to decompose at elevated temperatures to a liquid SiO_2 phase plus a crystalline metal oxide [5]. This suggests that pure zircon could, in principle, be used to form nanocrystalline metal oxide composites by direct high-temperature ion irradiation. An additional motivation for the study of radiation effects in $ZrSiO_4$ derives from the traditional importance of zircon in U-Pb geochronology [*e.g.*, see Refs. 6, 7] and from its more recent potential application as a storage or disposal medium for weapons-grade plutonium [8–10]. Second, we investigate the effects of irradiation on the microstructure of nanocrystals already formed by ion implantation. Unusual and unexpected microstructures for nanocrystals subjected to further ion bombardment are, in fact, found to be the rule rather than the exception. Appropriate selection of the implantation/irradiation conditions can, however, be used to simplify the near-surface nanocomposite microstructural properties or to intentionally produce novel microstructures with potential future applications in optical and other devices.

Relation to previous work

A number of techniques, including wet chemical synthesis [*e.g.*, Ref. 11], laser ablation [e.g., Ref. 12], and the chemical doping of glasses [13–16] have been shown to be effective methods for synthesizing nanocrystalline materials. The present work, however, focuses on the microstructure of nanocrystal-host systems formed either by ion implantation and thermal processing or directly by the irradiation of a suitable single-crystal phase. The synthesis of nanocrystals by ion implantation offers the important advantage of experimental flexibility over the other methods cited above, and the number of possible nanocrystal – host compositions that are accessible to ion-beam methods seems essentially unlimited. During the last decade, several research groups have used ion implantation to synthesize both metallic and semiconductor nanocrystals. In this way, discrete single-element nanoparticles of Cu [17, 18], Ag [19–21], Au [22–24], Fe [25], Pt [26], Pb [27], Se [28], Ge [29], and Si [30–33] have been formed. Compound nanocrystals have also been formed by sequential implantation of the constituent elements – these include InP [34], GaAs [35, 36], ZnS [37, 38], CdS [38, 39], CdSe [39–41] and PbS [38], as well as oxides such as VO_2 [42], V_2O_3 [43], and $ZnAl_2O_4$ [44]. Binary metallic alloy nanocrystals have also been synthesized [45, 46]. This list is not meant to be exhaustive, but is meant to give a feel for the versatility of the ion implantation technique to produce a large number of particle compositions. The number of reported studies of nanocrystals formed by implantation techniques is growing rapidly. In fact, many major materials- or irradiation-related conferences presently include entire symposia devoted to the formation of nanocrystals by ion implantation techniques.

Ion irradiation methods that do not involve significant implantation-produced chemical modifications have been less extensively investigated as a method for the formation of nanocrystals. The fact that new phases can form during the irradiation of metals and alloys has been known and documented for several decades [*e.g.*, see Ref. 47], and in the earth sciences, mineralogists have observed the occurrence of nanocrystalline monoclinic ZrO_2 in natural radiation-damaged zircon that contains uranium and thorium [*e.g.*, see Refs. 48, 49]. Irradiation of doped glasses may also lead to precipitate growth [50–53], and in this case, ionization-energy-loss processes are deemed responsible for the growth of the particles. Recently, researchers have investigated the formation of gold nanocrystals due to the ion irradiation of a pre-implanted host material [54]. In this case, the optical host is first implanted with gold at low temperatures so that the implanted material remains in solution in the near-surface region. The sample is subsequently irradiated by high-energy ions that pass through the pre-implanted region, causing the nucleation and growth of the gold particles.

The present work represents a systematic transmission electron microscope (TEM)-based study of the effects of irradiation on the formation of nanocrystals in either pre-implanted or directly irradiated materials. While the fact that ion implantation can be used to synthesize a large number of nanocrystal compositions is well established, the effects that the subsequent implantation can have on the resulting microstructures and size distributions are less well known. The present work shows how the effects of ion irradiation can, in fact, be used to good advantage in the formation of novel nanocrystal microstructures and nanocrystal-host structural relationships.

Experimental

The single-crystals of $ZrSiO_4$ and $ScPO_4$ investigated here were synthesized using a high-temperature-solution (flux) technique [55, 56]. The high-purity SiO_2 glass samples and [100]-oriented single crystal Si wafers were obtained commercially. TEM specimens for in-situ ion irradiations were prepared by conventional thinning methods [57]. The direct irradiation experiments were carried out using the HVEM-Tandem Facility at Argonne National

Laboratory. The specimens were irradiated with 800 keV Kr^+ ions, and the microstructural evolution was observed by standard bright-field imaging and electron-diffraction techniques. Details of the microscope and beam-line setup can be found elsewhere [57, 58]. The dose rate was 1.7×10^{12} ions/cm^2/s, and temperatures from –253°C up to 850°C were obtained by using a liquid-helium-cooled stage or a conventional resistive heating stage.

Ion irradiations and implantations were carried out at the Surface Modificaton and Characterization (SMAC) Facility at Oak Ridge National Laboratory. The specimens were mechanically clipped onto a steel backing plate, in some cases using graphite paint to provide a good thermal contact. Implantations were performed using a beam current density of less than 2 μA/cm^2 and the crystalline host materials were tilted approximately 7° off-axis to avoid ion-channeling effects. Thermal processing was carried out in a standard tube furnace in a reducing atmosphere.

Cross-sectional TEM specimens were prepared by gluing the implanted face onto a silicon wafer and hand polishing to a thickness of approximately 1–2 μm [59]. The samples were then ion milled at an angle of 12° for 15 to 45 min to expose the implanted surface. Conventional bright-field electron microscopy was performed using a Philips EM400 TEM operated at 100 keV. High-resolution imaging and Energy Dispersive X-ray Spectrometry (EDS) mapping was done with a Philips CM200 Scanning Transmission Electron Microscope (STEM). Electron energy loss spectroscopy (EELS) analysis was performed on a Philips CM30 operated at 300 keV and equipped with a Gatan Image Filter.

Results and discussion

Zircon and pretulite

Zircon and pretulite ($ScPO_4$) become amorphous at an ion dose that increases as a function of irradiation temperature (Fig. 1). The increase in the amorphization dose is a result of recrystallization processes that occur during irradiation that are enhanced at elevated temperatures. The amorphization dose for both compounds apparently increases in two relatively well-defined stages. Zircon can be amorphized at much higher temperatures than pretulite despite their similar ABO_4 stoichiometry and similar crystal structure. The activation energies for the annealing processes were calculated using a recently-developed model that relates the amorphization dose to temperature [60] and were found to be approximately 1.0 and 3.3 eV for the low-temperature and high-temperature annealing stages in zircon, respectively, and approximately 1.0 and 1.5 eV for the two stages in pretulite. The high-temperature activation energy for annealing in zircon (~3.3 eV) is reasonable for processes that occur above 700°C (Fig. 1). It is quite close to known values for the annealing of fission tracks in zircon (2.1 to 3.6 eV) [61] and it may, therefore, represent the annealing of bulk amorphous zones. The value obtained for the lower temperature process for both compounds (1.0 eV) is close to known interstitial and vacancy migration energies in MgO and Al_2O_3 as summarized in Ref. 62 and may be related to point defect recombination. The activation energy for Stage II annealing in pretulite is 1.5 eV. This low value (as compared to zircon) appears to be characteristic of phosphates in general [63, 64] and is consistent with the extreme rarity of metamict (*i.e.*, amorphous) uranium- and thorium-bearing phosphates in nature.

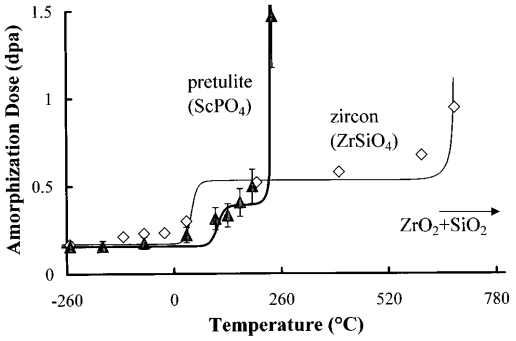

Fig. 1 Amorphization dose plotted as a function of temperature for zircon and pretulite irradiated with 800 keV Kr^+ ions. The lines represent the best fit to the experimental data obtained using the amorphization-recrystallization model derived in Ref. 60

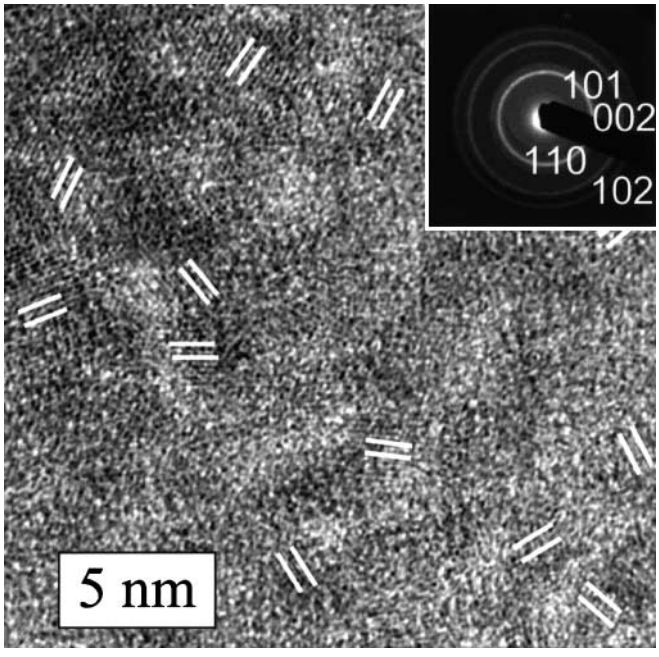

Fig. 2 Nanocrystals of cubic or tetragonal ZrO_2 embedded in amorphous SiO_2. This microstructure was produced by irradiating zircon to a dose of ~3 dpa at 800°C. The electron-diffraction pattern (inset) is indexed to tetragonal ZrO_2

In the case of the ion bombardment of zircon, a further effect occurs under irradiation at temperatures above 600°C. Between 600 and 750°C, zircon first becomes amorphous, but with increasing dose, it gradually decomposes into an assemblage of randomly oriented cubic or tetragonal ZrO_2 nanocrystals that are embedded in a matrix of amorphous SiO_2 (Fig. 2). The ZrO_2 precipitates are approximately 3 nm in diameter. Irradiation above 750°C leads to direct decomposition of zircon into the component oxides without the formation of an intermediate amorphous phase. Zircon specimens were irradiated at different temperatures and using different ion fluxes to ensure that the decomposition was not brought about by ion-beam heating [60].

The phases formed by the high-temperature ion-beam irradiation of zircon are the same as those that would be obtained by normal thermal melting, *i.e.*, $ZrSiO_4$ melts incongruently at 1960 K to form two phases: crystalline ZrO_2 and liquid SiO_2. Several authors have proposed that a so-called "cascade melting" phenomenon may account for the variation in the susceptibility of ceramics to ion-beam amorphization [65–67] but whether or not such a "cascade melting" phenomenon actually occurs in complex ceramics is not known. Clearly such a model is based on the assumption that the phase relationships inside the highly non-equilibrium cascade are at least qualitatively similar to those occurring at equilibrium. In any event, regardless of the nature of the responsible atomic-scale mechanisms, the experimental results for the high-temperature ion irradiation of zircon provide a clear example of how ion beams can be used to produce directly an assemblage of nanophase particles embedded in a ceramic host.

A phase decomposition similar to that characteristic of zircon does not occur for the case of pretulite. The orthophosphates melt directly to the liquid composition without the formation of intermediate solid-state phases. Another effect was observed in the case of pretulite, however. The ion-beam-damaged amorphous material was found to recrystallize rapidly under electron irradiation in the electron microscope. This remarkably rapid recrystallization led to a further set of experiments in which TEM specimens were irradiated to a dose of approximately twice the amorphization dose (*i.e.*, $2\times D_c$) while the electron beam from the microscope was turned off. The resulting amorphous regions were then irradiated using the electron beam in the TEM. The results were somewhat startling: the amorphous material recrystallized to form a nanometer-scale polycrystalline assemblage of $ScPO_4$ within a matter of seconds – depending on the beam-current density [68]. This crystallization could be controlled by focusing the electron beam and moving the focal point with the beam shift controls (Fig. 3). In this way, "letters" and patterns of nanocrystals could be drawn in the amorphous matrix. The size of the lettering depended only on the diameter of the electron beam and finer letters could be drawn by further focusing and reducing the TEM spot size. The calculated temperature rise due to beam heating was less than 40°C in these studies.

The mechanism responsible for the rapid recrystallization of $ScPO_4$ was investigated by performing irradiations using different accelerating voltages in the electron microscope. The dose for recrystallization was monitored by using a Faraday cup to obtain the beam current and by measuring the beam diameter on photographic negatives. The results are shown in Table 1: Clearly, increasing the electron energy causes an increase in the electron dose for complete recrystallization, as measured by electron diffraction. These results are consistent with an ionization-driven recrystallization mechanism [68]. The case of the electron irradiation of ion-beam-amorphized $ScPO_4$ provides an example of another "direct" radiation approach to the formation of crystalline nanophase precipitates in a host material. As compared with the case of zircon, however, here the host and precipitates are compositionally the same.

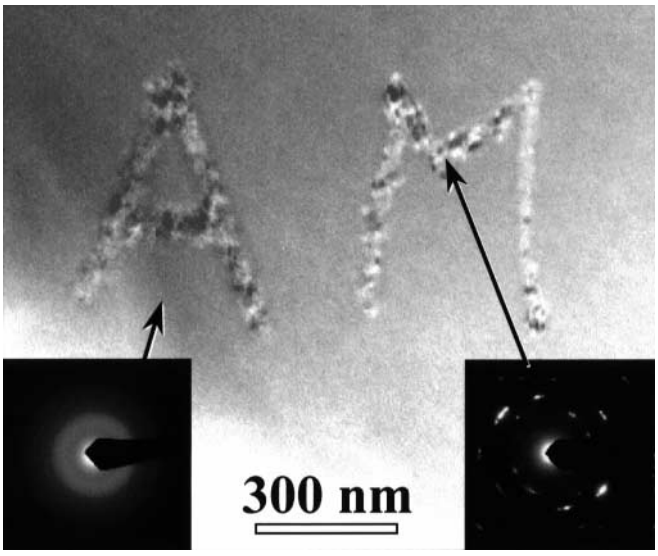

Fig. 3 Letters of crystalline pretulite "drawn" in an ion-beam-amorphized pretulite matrix. Crystallization was produced in-situ in the electron microscope by focusing the electron beam with the second condenser lens. The calculated temperature rise was less than 50°C

Table 1 Electron energy and dose for crystallization of $ScPO_4$

Energy (keV)	Crystallization Dose ($\times 10^{21}$ cm^{-2})
80	2.28
120	3.65
160	5.15
200	9.11
200	9.18

Formation of compound nanoparticles

The above two examples show that irradiation techniques can be directly used to produce nanocrystalline precipitate phases in a transparent host. In the case of pretulite, the spatial distribution of the nanocrystal precipitates could be controlled by selecting the area of the amorphous material that was to be subjected to electron irradiation. The formation of compound crystalline nanoparticles (*e.g.*, ZrO_2 embedded in SiO_2 in the zircon case) represents a further application of ion irradiation or implantation techniques; however, direct precipitation requires a specific set of circumstances which fortuitously exist in the case of zircon. Usually, it is necessary to sequentially implant the elements required to make up the nanocrystals, thereby producing an impurity supersaturation which can subsequently precipitate out of the

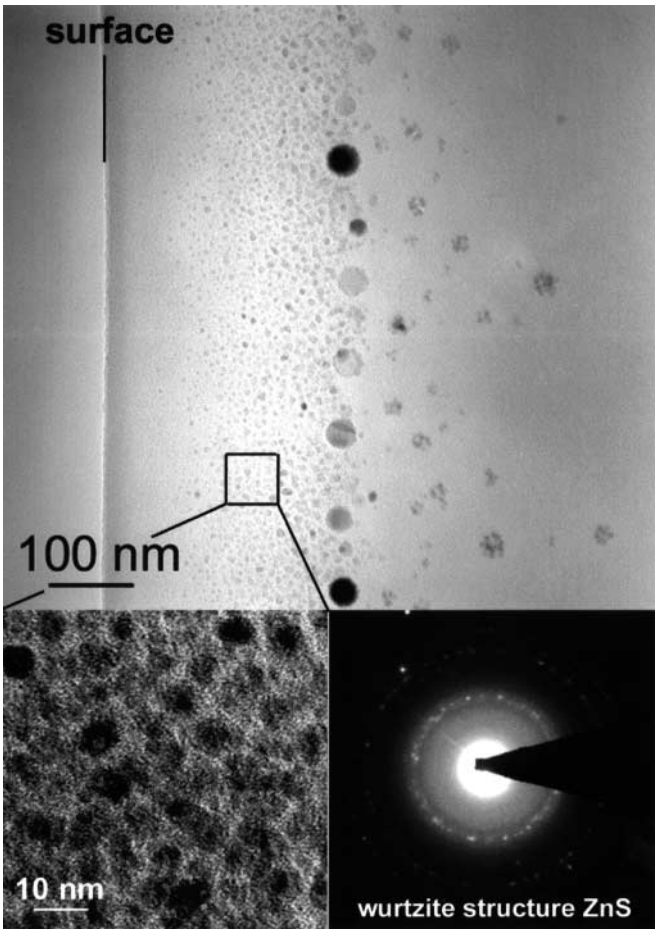

Fig. 4 Cross sectional TEM micrograph showing the distribution of wurtzite-structure ZnS precipitates produced by ion implantation into SiO_2 glass. The dose was 1×10^{17} ions/cm^2 for both elements, and the specimen was heated to 1000°C for 6 min in a reducing atmosphere

host as "nanocrystals" during thermal processing. This approach has been used to synthesize a number of II-VI and III-V semiconductor nanocrystals [38, 39, 69].

Radiation effects that occur in the host during implantation frequently complicate the overall microstructure and size distribution of the nanocrystals formed by thermal processing. For example, Fig. 4 shows semiconductor precipitates of ZnS formed in a fused silica host that was implanted at room temperature with 1×10^{17} ions/cm^2 of Zn (320 keV) followed by an equal dose of sulfur (180 keV). The implant energies were selected to give overlapping concentration profiles of the implanted species. The specimen was then annealed for 6 min at 1000°C under flowing Ar+4%H_2. Electron diffraction demonstrated the formation of randomly oriented wurtzite-structure ZnS precipitates, however, the nanocrystal size distribution is strongly bimodal. Calculations using the Monte Carlo computer code Transport and Range of Ions in Matter (TRIM v.96) [70] show that the SiO_2 glass should experience radiation damage up to a depth of ~300 nm, with a resulting conversion to the ion-beam-damaged structure (as opposed to "normal" SiO_2 glass structure) [71]. The location of the large precipitates corresponds to the calculated boundary between the radiation-damaged glass and the deeper region of the SiO_2 host that was not modified by the implantation. This bimodal size distribution is generally undesirable for device applications and is a negative consequence of the irradiation process. Similar distributions of ZnS precipitates in SiO_2 glass have previously been observed [37, 38], and this poor size distribution is probably responsible for the lack of well-defined absorption features associated with quantum-confined particles.

Irradiation-induced nucleation of ZnS nanocrystals

The results discussed here for the case of pretulite suggest that, in principle, electron irradiation might also be used to nucleate isolated, monodispersed nanocrystals of ion-implanted species. To test this concept, an SiO_2 glass wafer was implanted with 1×10^{17} ions/cm^2 of zinc (320 keV) followed by an equal dose of sulfur (180 keV). ZnS was chosen as the target composition because our previous experiments demonstrated that Zn and S have a strong affinity and will readily react to form the sulfide [38]. The specimens were heat sunk during implantation to prevent nanocrystal nucleation prior to the electron irradiation step. Cross-sectional specimens were then prepared for in-situ electron irradiation in the TEM.

In the as-implanted sample, crystalline ZnS precipitates were not observed in the implanted region. After 60 s of irradiation with 200 keV electrons (beam current density = ~1 A/cm^2), however, regions of dark contrast were observed that were tentatively ascribed to Zn-rich areas (see Fig. 5). With increasing electron dose in the TEM, these dark regions became more distinct. After 10 min of irradiation, electron diffraction and high-resolution imaging clearly demonstrated the formation of discrete ZnS precipitates with an average diameter of 3.1 nm (Fig. 5). The standard deviation in the precipitate size is 0.45 nm – considerably smaller than for the ZnS particles produced by high-temperature annealing (*e.g.*, see Fig. 4). In fact, this technique produces what is apparently the narrowest reported size distribution of compound nanocrystals formed by implantation techniques.

Specimen heating caused by the electron beam might enhance the crystallization process, however, the temperature rise for the irradiation conditions appropriate to Fig. 5 was calculated using Fisher's model [72] to be less than 40°C. Further evidence that electron-beam heating plays only a minor role is provided by the observation that the size of the precipitated ZnS particles was uniform throughout the entire irradiated region. If specimen heating were important, then the larger particles would be expected to form near the center of the electron beam profile where the temperature is highest, but this effect was not observed.

Recent work has shown that MeV ion irradiation can be used to nucleate gold precipitates in SiO_2 glass specimens pre-implanted with gold [54] and that silver intro-

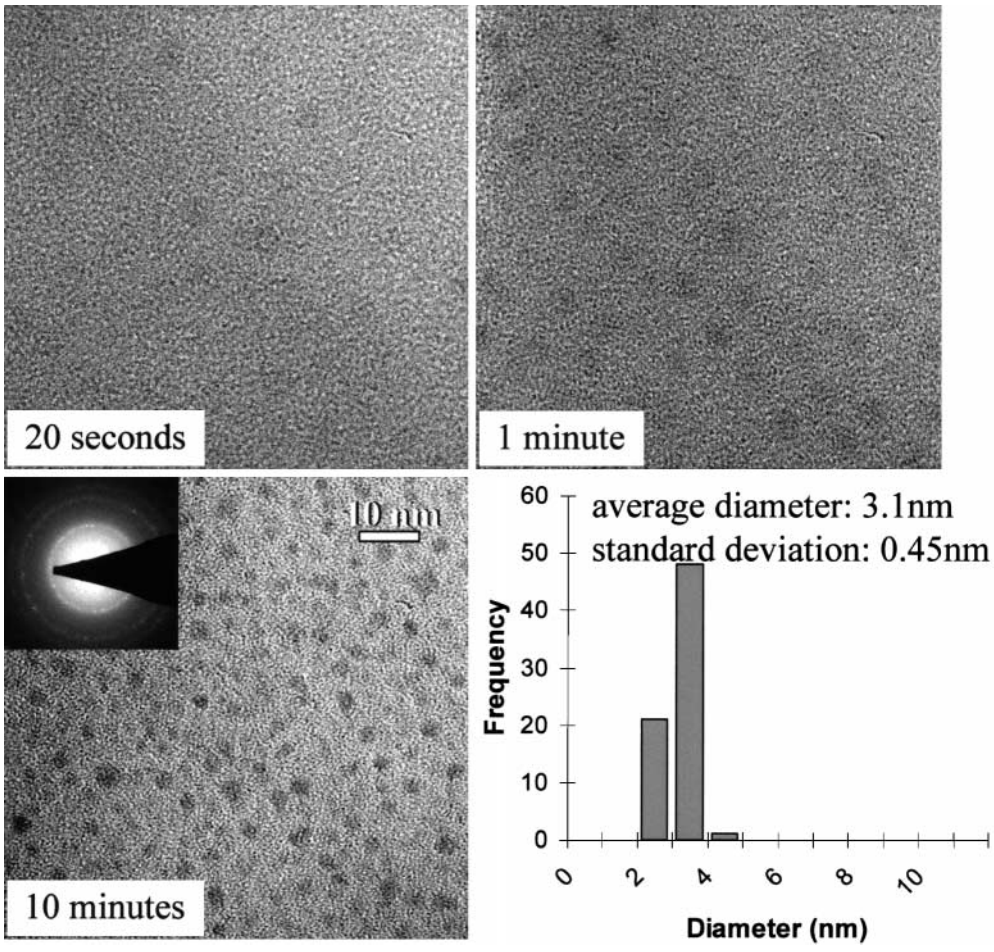

Fig. 5 Electron-irradiation-induced nucleation and growth of zincblende-structure ZnS nanocrystals in SiO_2 glass. The specimen was implanted under the same conditions as the specimen in Fig. 4, except that the sample was heat sunk during implantation and was not thermally annealed. The beam current was approximately 1 nA. The size distribution histogram is given on the bottom right

duced into glass via ion exchange also precipitates out of solution during subsequent ion irradiation [52]. In both of these cases, electronic-energy-loss processes were deemed to be responsible for the growth of the metal precipitates. As an extension of the results reported for Au and Ag, we attempted to nucleate and grow compound nanocrystals of ZnS by ion irradiation of material that was previously implanted with Zn and S. Specifically, a specimen of SiO_2 was implanted with Zn+S at liquid nitrogen temperature to a dose of 1×10^{17} ions/cm^2 (exactly as described above for the electron-irradiation case). This sample was subsequently irradiated at 250°C using 6.7 MeV Si^{3+} to a fluence of 1.0×10^{16} ions/cm^2. These high energies were chosen in order to obtain a high electronic stopping power for the Si ions in the pre-implanted region. The resulting microstructure was then examined by cross-sectional TEM.

In the case of the pre-implanted specimen irradiated with silicon, the resulting microstructure was completely different from that observed after the thermal annealing of Zn+S-implanted SiO_2 glass wafers. The microstructure consists of three zones that are, in order of increasing depth: very small (*e.g.*, 2–4 nm) spherical ZnS precipitates; ZnS precipitates elongated perpendicular to the specimen surface; and finally, another layer of small, spherical precipitates (Fig. 6). The elongated precipitates are, in some regions, continuous for up to 100 nm. Electron diffraction confirmed the zincblende structure for these nanocrystals.

This layered microstructure is apparently related to the initial distribution of the Zn and S. The RBS results in Fig. 7 show that the layer of elongated precipitates occurs where the concentration of implanted zinc is greater than ~3.7×10^{21} ions/cm^3. The measured concentration profile of the implanted Zn is significantly wider than would be expected on the basis of TRIM calculations. The long axis of the precipitates is parallel to the implantation/irradiation direction. The Si ions may actually nucleate ZnS nanoparticles along their ion tracks. Because of the relatively high concentration of implanted silicon, the elongated particles could have formed along individual ion tracks or they may have crystallized as a result of multiple ion track overlaps.

Annealing of the Si-irradiated specimen at 1000°C for 1 h results in a further microstructural “layering” effect. The elongated particles were still present (Fig. 8), but three bands of larger, wurtzite-structure ZnS precipitates formed at depths of 30, 100, and 260 nm, respectively (*i.e.*, at the near-surface and at the boundaries of the layer with the elongated particles). Isolated ZnS precipitates were also observed at depths ranging from 300 to 600 nm. This observation is consistent with the enhanced

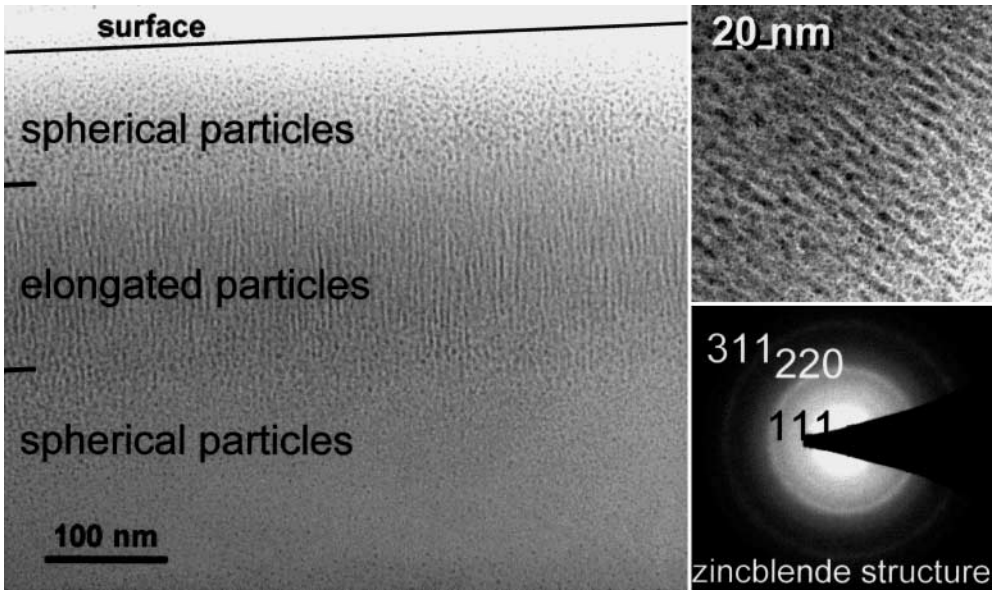

Fig. 6 Cross-sectional micrograph showing the structure of ZnS precipitates formed by Si-ion-irradiation of ion-implanted SiO_2 glass. A representative diffraction pattern and a higher-magnification image of the elongated particles are given on the right. The specimen was first implanted with Zn+S exactly as described for Fig. 5 and it was then irradiated with 6.7 MeV Si ions at 250°C to a dose of 1×10^{16} ions/cm^2

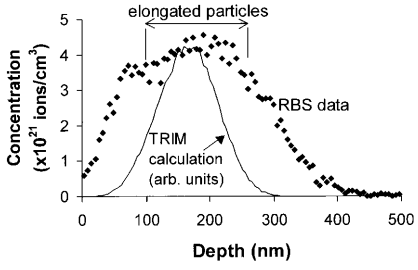

Fig. 7 Depth distribution profile for implanted Zn after a subsequent 6.7 MeV Si irradiation. The distribution obtained by TRIM-96 calculations is shown for comparison. The elongated particles occur over an observed depth range corresponding to an implanted Zn concentration greater than approximately 4×10^{21} ions/cm^3. The sulfur distribution is similar to that for zinc but the scatter in the data is considerably larger owing to its low atomic mass

diffusion of Zn and S in radiation-damaged fused silica glass. These results clearly show that the microstructure of semiconductor nanocrystals formed by ion implantation can be controlled to some extent and modified by a selection of the implantation/annealing conditions.

It should be noted that gold nanoclusters can also be formed by an implantation/irradiation process. When porous vycor specimens are immersed in a methanol solution containing 0.01 M $NaAuCl_4$, low concentrations of gold complexes remain in the porous glass after drying in air [73]. TEM specimens were prepared from this material and were irradiated by 60 or 200 keV electrons in the electron microscope under conditions similar to those described above in the case of ZnS. Electron irradiation causes the pores to collapse and Au nanoparticles to precipitate (Fig. 9). The amount of energy transferred to a gold atom by a 60 keV electron is less than 0.8 eV. This is probably too low to displace gold atoms by ballistic collision processes. The calculated net dose was lower for the 60 keV irradiations than for the 200 keV irradiations, consistent with an ionization-related process.

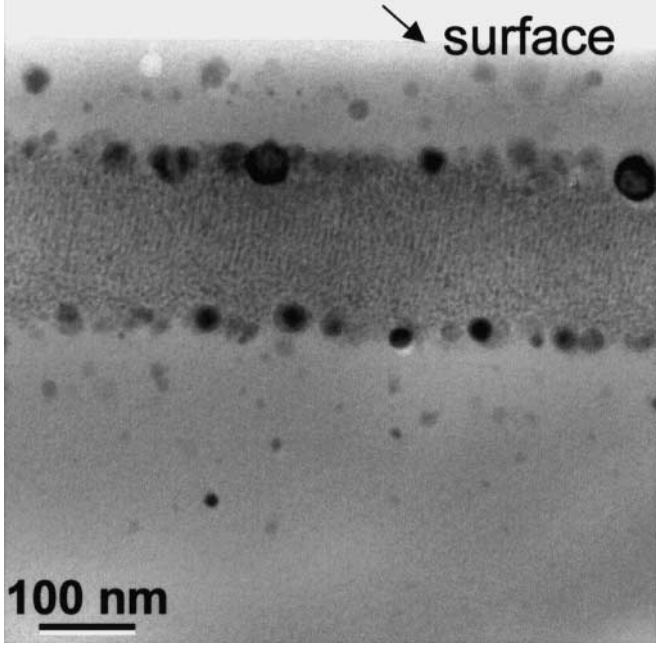

Fig. 8 Cross-sectional micrograph of the specimen shown in Fig. 7 after thermal annealing for 1 h at 1000°C in flowing Ar + 4%H_2

Formation of coherent, oriented ZnS particles in amorphous Si

We recently reported a technique by which coherent, crystallographically oriented nanoparticles can be produced in an amorphous host material [74] – an additional example of the use of ion-beam methods to create unusual microstructures. In order to synthesize oriented crystalline particles in an amorphous host, the host should be resistant to amorphization at elevated temperatures but must be relatively susceptible to irradiation-induced amorphization at low temperatures. The nanocrystals

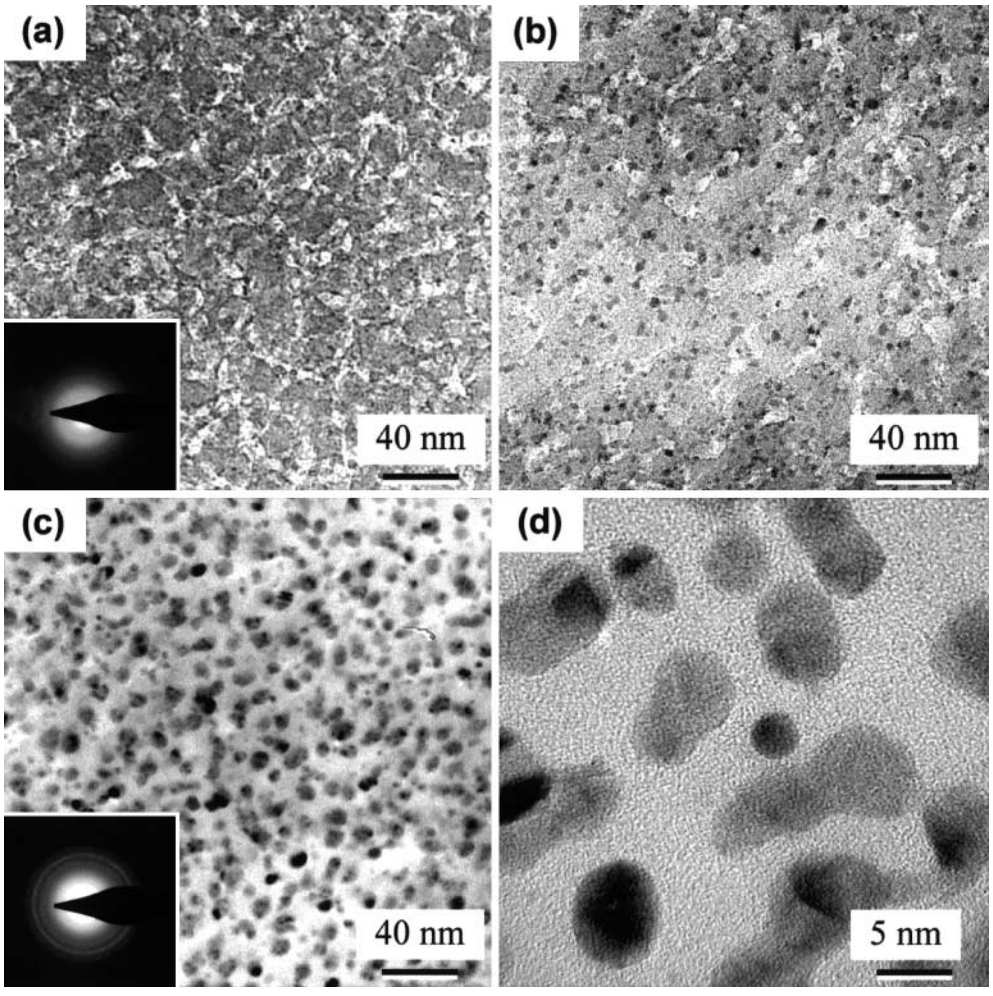

Fig. 9 Electron-irradiation-induced nucleation of gold nanocrystals in gold-impregnated vycor. Panels (c) and (d) were obtained after approximately 5 min of irradiation using a beam current of 1 nA

must crystallize in the selected crystalline host at high temperatures and should be highly radiation resistant at all temperatures. In this method, ion implantation and thermal processing are first used to form nanocrystal precipitates that are coherently oriented with respect to a crystalline host. The host material is then amorphized by ion irradiation leaving the highly radiation resistant precipitates in an aligned crystalline state.

In order to identify a host material with the appropriate properties noted above, the simple oxides MgO, Al_2O_3, and SiO_2 as well as Si, $LaPO_4$, and $SrTiO_3$ were tested as candidate host materials by in-situ irradiation using the HVEM-Tandem Facility. The irradiation conditions were as described previously for zircon and pretulite. The best candidate hosts were found to be Si and $SrTiO_3$ (Fig. 10). ZnS was selected as the target nanocrystal composition because of its resistance to irradiation-induced amorphization [75]. When formed by ion implantation into crystalline hosts (as opposed to fused silica), ZnS nanocrystals are generally faceted and are crystallographically aligned with respect to the matrix. [38]. Si was selected as the host material for these experiments because of the close lattice match with the zinc-blende structure of ZnS. The Si host crystal was first implanted with Zn (280 keV) and S (160 keV) to a dose of 5×10^{16} ions/cm^2. The temperature during implantation was maintained at 550°C in order to prevent amorphization of the silicon host. The specimens were then annealed at 1000°C for one hour in flowing Ar+4%H_2. X-ray diffraction analysis indicated the presence of zinc-

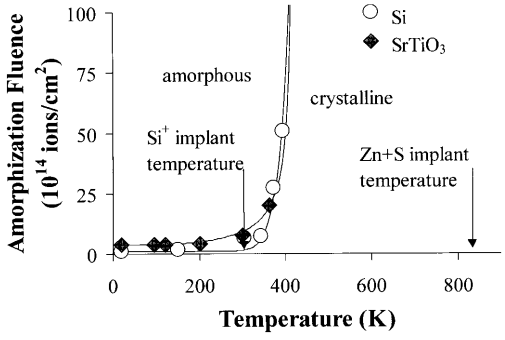

Fig. 10 Amorphization dose as a function of temperature for $SrTiO_3$ and Si. The data were obtained by irradiating thin specimens in-situ at the HVEM-Tandem Facility using 800 keV Kr^+ ions (as in Fig. 1). Si and $SrTiO_3$ can be amorphized readily at low temperatures but cannot be amorphized above ~200°C

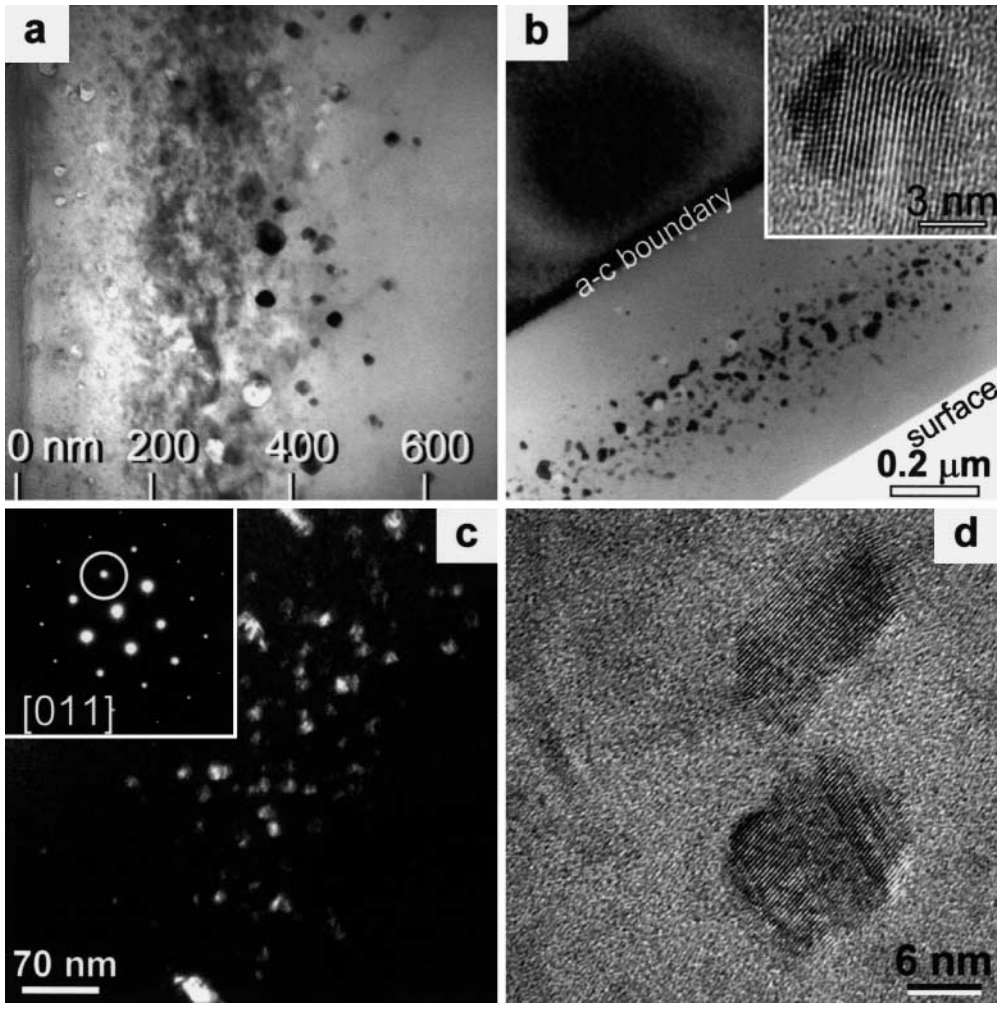

Fig. 11 Oriented ZnS nanocrystals in (a): crystalline and (b): ion-beam-amorphized silicon. A (111) dark-field image of the amorphized silicon is shown in (c). The ZnS precipitates all appear bright – indicating that they are crystalline and coherently aligned in the amorphous matrix. A high-resolution image is shown in (d). The lattice fringes in adjacent precipitates have the same orientation

blende-structure ZnS particles aligned "cube-on-cube" with the host silicon lattice. A band of faceted and crystallographically oriented ZnS nanocrystals centered around a depth of 250 nm was observed by cross-sectional TEM (Fig. 11a). The specimen was then irradiated with Si^+ ions at liquid nitrogen temperatures using a range of ion energies to ensure a uniform amorphous layer. TEM analysis showed that the Si was indeed amorphized up to a depth of 750 nm (Fig. 11b). In contrast, the radiation-resistant ZnS precipitates remained crystalline. The dark-field image in Fig. 11c shows that all the nanoparticles simultaneously diffract into the Si (111) beam (equivalent to the (111) beam for ZnS) – demonstrating that they remain crystallographically aligned and oriented even though the host silicon is amorphous. High-resolution imaging also showed that the precipitates were aligned (parallel lattice fringes) and, frequently, twinned (Fig. 11d).

By exploiting the flexibility of ion implantation and the intrinsic differences in the recrystallization behavior between potential host materials and various types of nanophase precipitates, it is possible, in principle, to achieve a wide range of surface nanocomposite systems consisting of various types of oriented crystalline particles embedded in an amorphous matrix. New effects associated with the crystallographic particulate orientation and/or morphology are anticipated in surface nanocomposite systems of this type.

Hollow nanocrystals

The possibility of using implantation to intentionally form novel and unusual microstructures is further illustrated by recent observations of nanoparticles containing internal light-contrast features (as observed by conventional bright-field TEM). These recent observations include what are apparently hollow precipitates of mercury embedded in steel [76] and $MoSi_2$ precipitates in implanted silicon [77]. An examination of bright-field TEM images published in previous work [78] also suggests the presence of internal voids in GaAs nanocrystals, although this microstructure was not investigated or commented on at the time.

Recently, we have obtained clear evidence for the existence of hollow CdS precipitates formed by ion implantation and thermal processing [38]. One example of such a precipitate is shown in Fig. 12. A light contrast feature is clearly visible across the central portion of the nano-

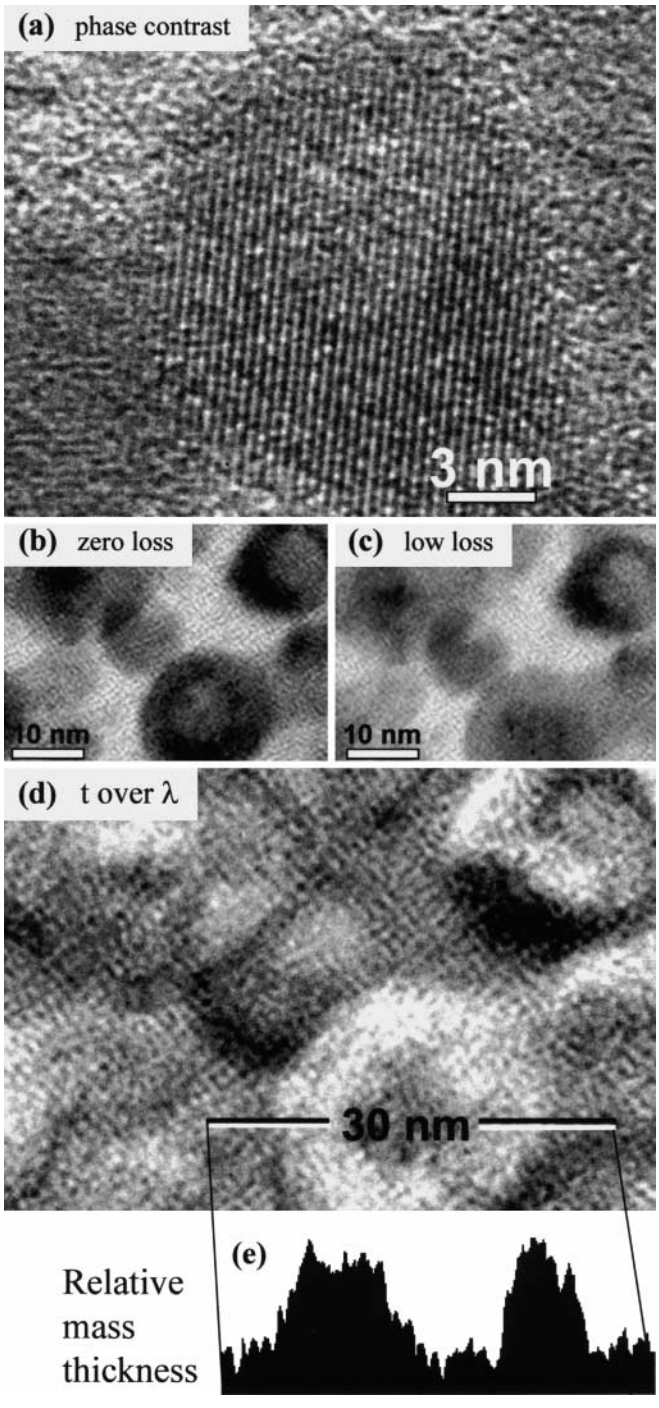

Fig. 12 (a): High-resolution image of a CdS precipitate in SiO_2 glass. There is a light-contrast feature in the center of the nanocrystal. The specimen from which this image was obtained was implanted to obtain a local concentration of 5.3×10^{21} ions/cm^3. Panels (b) and (c) are zero-loss and low-loss EELS images and (d) is a t-over-λ map (see text). Panel (e) shows a mass thickness (intensity) profile across the large precipitate in (d)

particle. EELS imaging was used to confirm that this feature is actually void (Fig. 12). Both "zero-loss" and "low-loss" images were acquired from a region of the specimen containing the "ring-shaped" nanoparticle images. The zero-loss image was formed by allowing only a narrow energy band of electrons centered about the zero-energy-loss position to form the image, so that the inelastically scattered plasmon-loss and core-loss electrons are excluded. The low-loss image is acquired with the slit removed, so that both zero-loss and inelastically scattered electrons are used to form the image. A measure of the local mass thickness is given by the relation: $t/\lambda=ln(I_L/I_0)$, where t is the thickness of the specimen, λ is the mean free path for inelastic scattering, and I_0 and I_L are the intensities in the zero-loss and low-loss images, respectively. Typically, the mean free path is smaller for materials of higher atomic number, and t/λ is, therefore, correspondingly higher for a constant specimen thickness. A "t-over-λ map" is shown in Fig. 12, as well as a profile of t/λ across the ring-shaped particle image. The mass thickness is clearly higher when the beam passes through the side walls of the particle, but the mass thickness in the center of the particle is similar to the surrounding matrix. Given that, at the center of the particle, the beam probably passes through the ~5-nm-thick top and bottom surfaces of the higher-density particles, it follows that the core of the particles must be of a much smaller mass thickness than the surrounding matrix. These light-contrast features are, therefore, likely to be voids or bubbles, and the ring-shaped images actually represent hollow spheres. This hypothesis is in agreement with the consistently light diffraction contrast from the center of the nanocrystals. The formation of hollow nanoparticles offers an opportunity for further materials engineering, whereby the central portions of the nanocrystals might, for example, be filled with another material.

Potential origins of the central voids include radiation-induced vacancy aggregation and coalescence, volume changes associated with solid-liquid or solid-solid transformations, adsorption of gas atoms at void sites in the crystalline lattice, or a combination of these processes. In order to investigate the mechanism of void formation, we synthesized additional CdS and ZnS precipitates by implantation and thermal processing. After each processing step, the specimen was examined by cross-sectional electron microscopy. SiO_2 glass wafers were first implanted with Cd or Zn to a dose of 1×10^{17} ions/cm^2. The implantations were carried out at room temperature, and the specimens were not heat sunk. The beam current density was less than 2 μA/cm^2, as in all the experiments described above. Cross sectional TEM investigations demonstrated the presence of randomly oriented, spherical Zn or Cd particles ranging in size from 1 to 4 nm in diameter (*e.g.*, see Fig. 13a for the case of Zn nanocrystals). The metal nanocrystals do not contain internal voids or any other unusual characteristics. Next, an equal dose of sulfur was implanted into both specimens under identical implantation conditions. TEM observations after the sulfur implantation showed that the previously existing metal nanoparticles reacted to form the sulfide composition (Fig. 13b). The zincblende-structure sulfide particles contain distinct central void features.

The specimens were then annealed at 1000°C for 1 h in a reducing environment. In the case of ZnS, the size-

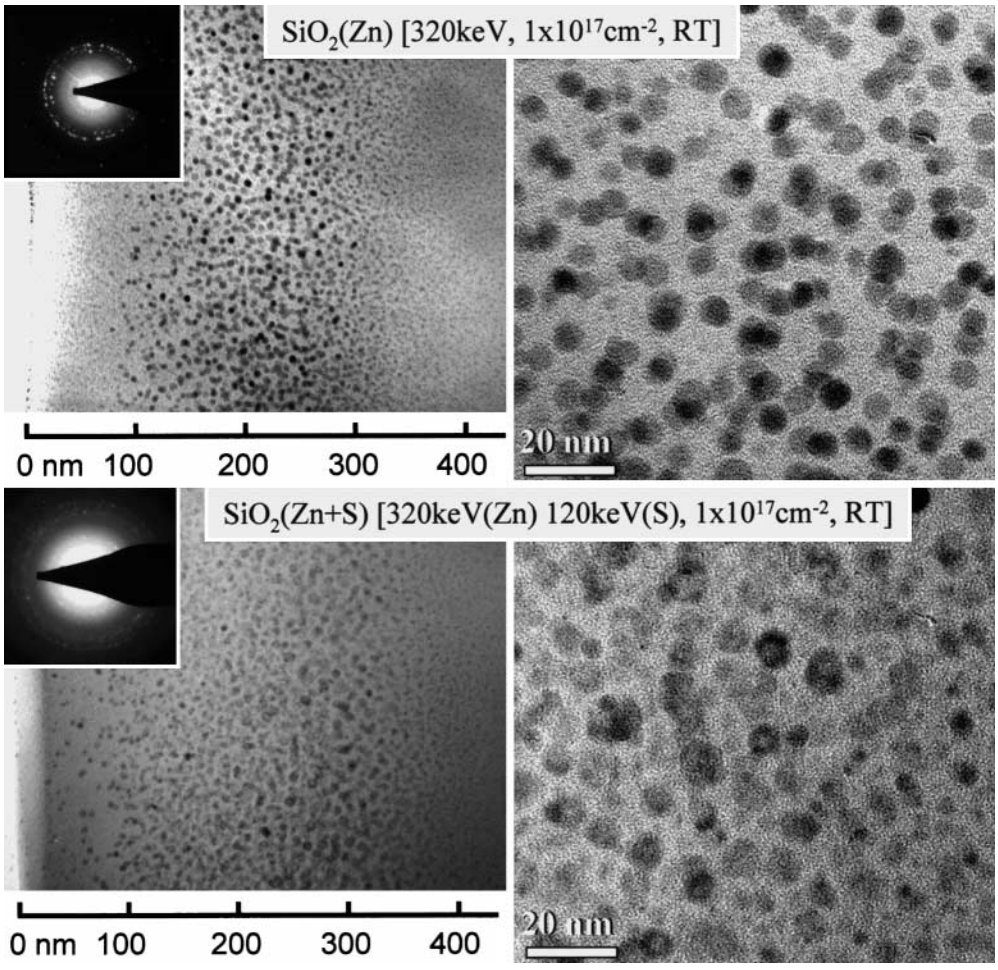

Fig. 13 Cross-sectional and high-magnification TEM micrographs showing the evolution of the precipitates during implantation at room temperature. An SiO_2 specimen was first implanted with 1×10^{17} ions/cm^2 of Zn at 320 keV (top). Randomly oriented spherical colloids of metallic Zn occur throughout the implanted region. The Zn colloids react with subsequently implanted sulfur (180 keV) to form zincblende-structure ZnS (bottom), and many of the sulfide particles are hollow

layering effect occurred, where the large particles were located at the maximum extent of the ion-irradiation-damaged glass and only a few of the smaller ZnS particles were hollow. The size-layering effect suggests that significant diffusion and re-precipitation of the implanted material has occurred. On the other hand, most of the CdS particles were clearly hollow as shown in Fig. 12, and in fact, the distribution of hollow particles reflected the concentration of the implanted material. A final experiment was carried out in which an SiO_2 glass wafer was implanted with Cd+S at liquid nitrogen temperature (all other experimental conditions were identical to those for the previous samples). After implantation and annealing (1000°C, 1 h), CdS nanocrystals were present in the implanted layer but they were not hollow (Fig. 14).

The above observations eliminate radiation damage alone as the origin of the voids. If radiation-induced vacancy aggregation and coalescence were responsible for the large internal voids, then we would expect to see voids in the metal nanoparticles that form *during* implantation, and this is not observed. Instead, the voids develop during the implantation of sulfur. Volume shrinkage associated with the metal to sulfide transformation is also not considered to be a likely source for the voids because the molar volume of the sulfide (CdS or

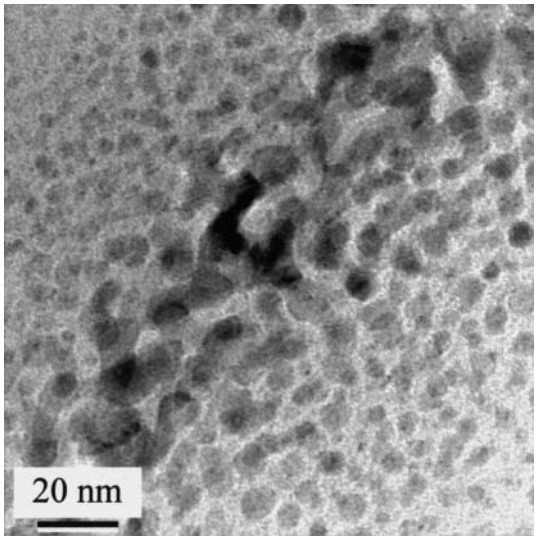

Fig. 14 Cross-sectional micrograph showing CdS precipitates in SiO_2 glass. The specimen was implanted to a dose of 7.5×10^{16} ions/cm^2 at energies of 320 keV (Cd) and 115 keV (S). The specimen was heat sunk during the implantation. Hollow nanocrystals are not observed

ZnS) is larger than that for the pure metal. The melting temperature of ZnS and CdS is considerably higher than the annealing temperature, so a volume change due to solidification of the liquid phase is not responsible for the formation of the voids – although we have recently obtained evidence that this effect can play a major role in the formation of hollow or void-containing metal precipitates embedded in crystalline silicon.

These observations suggest that the implanted sulfur is associated with the hollow particle formation. A possible explanation for the occurrence of hollow particles involves sulfur adsorption at defects in the crystalline lattice of the pre-existing metal (or semiconductor) colloids. If the vapor pressure of the implanted sulfur is sufficiently high, then the sulfur could adsorb onto vacancy embryos that form during irradiation. The vapor pressure of sulfur is approximately 0.13 kPa at the irradiation temperatures employed here [79]. During irradiation, the lowest energy location for sulfur atoms is on crystalline metal or semiconductor surfaces (*i.e.*, voids in the metallic precipitates) [*e.g.*, see Refs. 80 and 81 for examples of sulfur adsorption on metal surfaces]. A similar process has been invoked to explain the formation of voids in ion-irradiated metals [82] and a large literature exists for the formation of voids by gas-ion irradiation into crystalline silicon [83–89]. If the local sulfur concentration is sufficiently high (*e.g.*, at the peak implanted concentration profile), then sulfur atoms may preferentially adsorb on vacancy embryos in the crystal lattice of the pre-existing metal colloids. At low implant temperatures, the vapor pressure would be too low for significant surface adsorption of sulfur to occur. Other low-boiling point or high vapor pressure elements would be expected to have similar effects; hence the apparent voids shown in Fig. 1b of Ref. 78 for the case of GaAs in SiO_2.

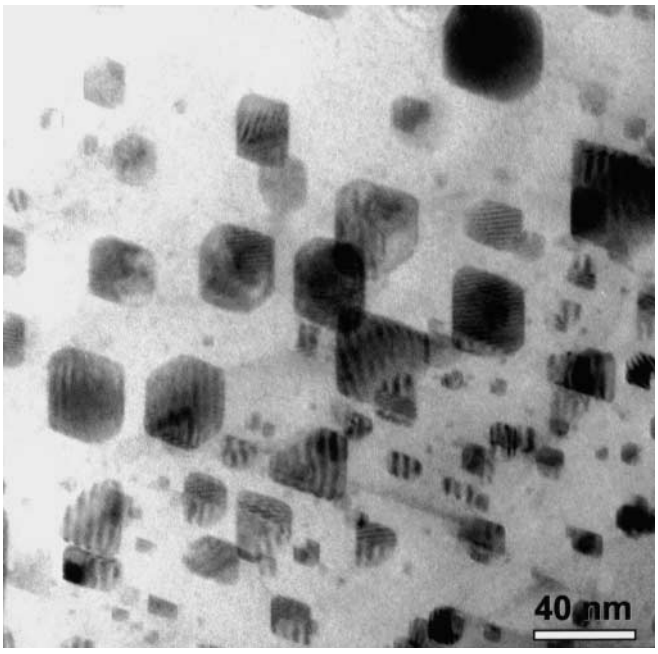

Fig. 15 Cross-sectional micrograph showing CdS precipitates in (100)-oriented crystalline silicon. The viewing direction is approximately 10° off the [110] zone axis. The silicon was implanted at 550°C to a dose of 4.3×10^{16} ions/cm^2 using ion energies of 410 keV (Cd) and 150 keV (S). The sample was then annealed for 1 hour at 1000°C in Ar + 4%H_2

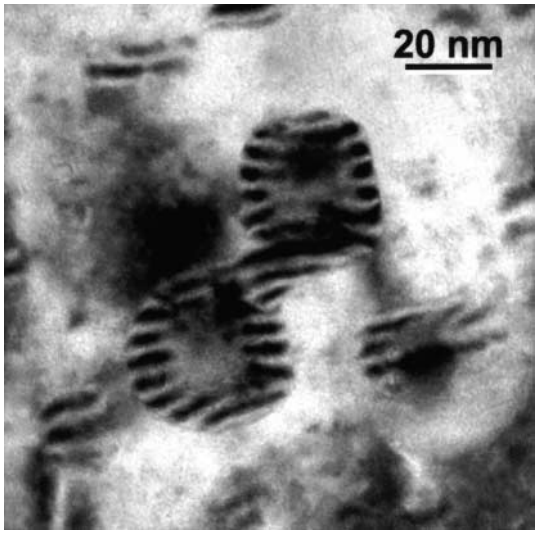

Fig. 16 Plan-view micrograph of the precipitates in Fig. 15 after subsequent implantation of Zn+S followed by a second thermal processing step at 1000°C. The two large particles are hollow and connected by a neck

Mixed chalcogenide nanocrystals

Finally, we report our initial results on the use of ion implantation to form mixed chalcogenide nanostructures. Previous work [39] indicated that nanocrystals with a composition close to $CdSe_{0.5}S_{0.5}$ could be formed by the stoichiometric implantation of the constituent elements followed by thermal processing. Evidence for the formation of a mixed chalcogenide composition was obtained by X-ray diffraction, which indicated a lattice parameter for the mixed nanocrystals that was smaller than that for pure CdSe– but larger than that of CdS.

In the present work, we have obtained direct TEM evidence for the formation of a mixed chalcogenide composition (Cd,Zn)S, with a ratio of Zn and Cd close to 1:1. This was accomplished by using a slightly different technique than for the mixed-anion composition Cd(Se,S) discussed above. Cadmium and sulfur were first implanted at 550°C into a (100)-oriented Si wafer (dose for each ion: 4×10^{16} ions/cm^2). The specimen was then annealed at 1000°C for 1 h in flowing Ar + 4% H_2 to form discrete CdS precipitates (Fig. 15). The sample was then implanted with an additional 4×10^{16} ions/cm^2 of both Zn and S, again at 550°C to prevent amorphization of the silicon. The specimen was subsequently annealed for an additional hour. Mixed chalcogenides or "core-shell" structures were considered to be possible results.

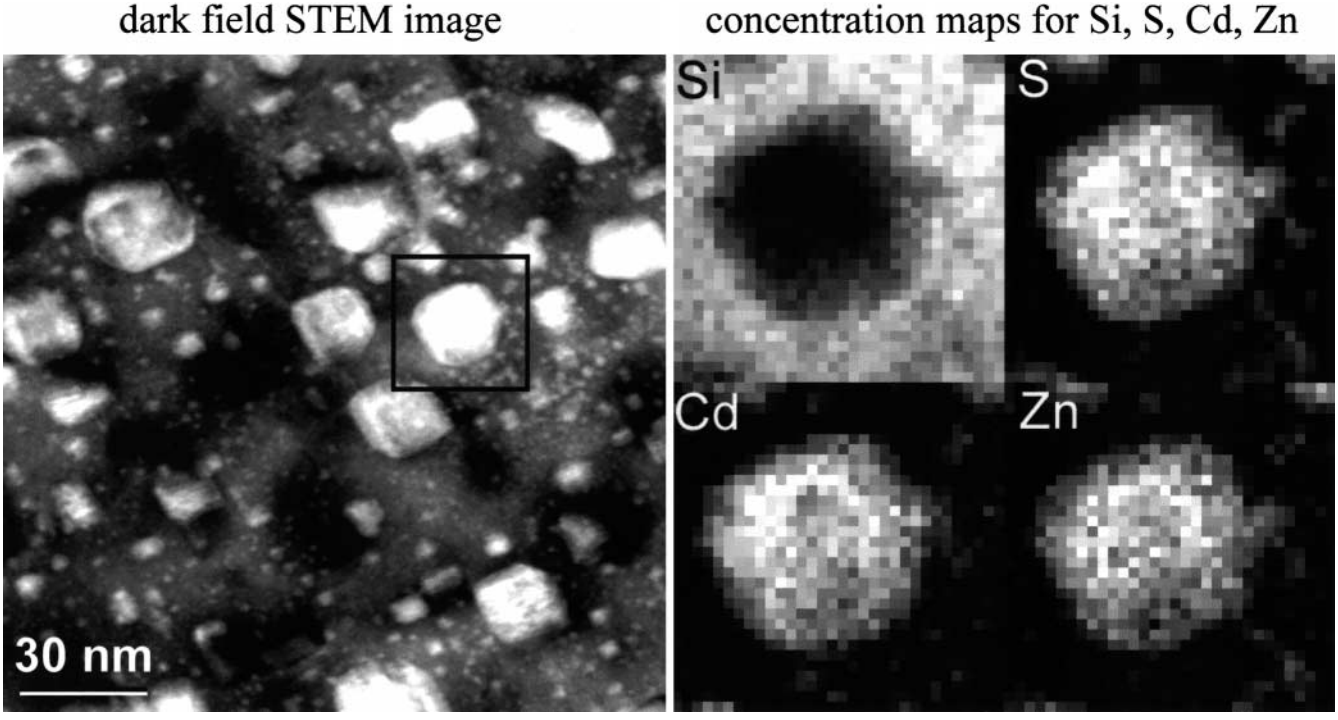

Fig. 17 Left: A dark-field STEM image of the CdS-ZnS precipitates. The beam was step scanned across the area marked by the box, and an EDS spectrum was collected at each pixel. The resulting elemental maps for Si, S, Zn, and Cd are shown on the right

Figure 16 shows that the resulting particles are crystalline, as evidenced by the pronounced Moiré fringe contrast. The particles appear as cubes in this plan-view image, although Fig. 15 shows that they are actually octahedra with apices pointing in the 100 directions of the silicon. Many of the precipitates contain internal void features. The distribution of Cd, Zn, and S within the particles was obtained by an EDS mapping technique using the electron microscope in the STEM mode. A dark field STEM image of the nanocrystals embedded in silicon is shown in Fig. 17. One of the precipitates (marked by the box) was then selected for elemental mapping.

In order to obtain an elemental map, the beam was rastered in 32 steps across the area within the box. The dwell time at each step was 0.5 s. Specimen drift was corrected automatically by scanning a separate reference area after each 64th pixel. The results, in the form of elemental maps for silicon, sulfur, zinc, and cadmium are shown in Fig. 17. No silicon was detected within the particle, nor was any Zn, Cd, or S found outside it. The Cd, Zn, and S occur essentially in the same regions of the particle, with high concentrations of Zn corresponding to high concentrations of Cd. These results show that a mixed composition close to $Cd_{0.5}Zn_{0.5}S$ has been formed. Presumably, the annealing temperature of 1000°C is sufficiently high for the diffusion of the implanted zinc and sulfur into and throughout the preformed CdS precipitates. These results show that multicomponent solid-solution nanocrystal compositions can be formed by ion implantation techniques.

Summary

The present work has focused on the effects of displacive and ionizing irradiation on the ABO_4 compounds zircon and pretulite. Zircon undergoes a radiation-induced phase decomposition to its component oxides with the resulting phase assemblage consisting of randomly oriented ZrO_2 nanocrystals in a matrix of amorphous SiO_2. Pretulite, an isostructural phosphate analogue of zircon, cannot be amorphized at elevated temperatures, and, in fact, it can be made to recrystallize as a result of low-energy electron irradiation – a process which could find applications in electron lithography. Electron irradiation can be used to induce the precipitation of ZnS in fused silica, and this technique, if applicable to bulk samples, could be used to form precipitates of a more uniform size – a goal thus far not achieved by ion implantation processes. Combinations of implantation and irradiation techniques can be used to form novel near-surface microstructures, as illustrated by the cases of hollow CdS nanocrystals and oriented ZnS nanocrystals produced in an amorphous host material. Solid solution or “alloy” nanocrystal precipitate compositions can also be formed. These results demonstrate the overall flexibility of implantation/irradiation techniques for producing unique microstructural property relationships between embedded nanocrystals and their hosts.

Acknowledgements A.M. acknowledges support from the NSERC (Canada). Electron microscopy was performed at the HVEM Tandem Facility at ANL and at the ShaRE Facility at ORNL. Ray Zuhr and Ed Sonder performed some of the ion implantations. Jim Bentley and Ian Anderson are thanked for providing assistance and training in the use of the STEM. Oak Ridge National Laboratory is managed by Lockheed Martin Energy Research Corp. for the U.S. Department of Energy under contract number DE-AC05-96OR22464.

References

1. Faraday M (1857) Proc Roy Soc, London 8:356
2. Mie G (1908) Annalen der Physik 25:377
3. Chan WCW, Nie S (1998) Science 281:2016
4. Bruchez M, Morrona M, Gin P, Weiss S, Alivisatos AP (1998) Science 281:2013
5. Butterman WC, Foster WR (1967) Am Mineral 52:884
6. Krogh TE (1982) Geochim Cosmochim Acta 46:637
7. Heaman L, Parrish RR (1991) In: Heaman L, Ludden JN (eds) Applications of radiogenic isotope systems to problems in geology: MAC Short Course Volume 19, Mineralogical Association of Canada, Toronto, Ont., p 59
8. Burakov BE, Anderson EB, Rovsha VS, Ushakov SV, Ewing RC, Lutze W, Weber WJ (1996) In: Murphy WM, Knecht DA (eds) Scientific basis for nuclear waste management XIX, Mat Res Soc Symp Proc Vol 412. Materials Research Society, Pittsburgh, PA, p 33
9. Ewing RC, Lutze W, Weber WJ (1995) J Mater Res 10:243
10. Ewing RC, Weber WJ, Lutze W (1996) In: Merz ER, Walte CE (eds) Crystalline ceramics: waste forms for the disposal of weapons plutonium. NATO Workshop Proceedings, Academic Publishers, Dordrecht, The Netherlands, p 65
11. Hines MA, Guyot-Sionnest P (1996) J Phys Chem 100:468
12. Serna R, Missana T, Alfonso CN, Ballesteros JM, Petford-Long AK, Doole RC (1998) Appl Phys 66:43
13. Doremus RH (1963) J Chem Phys 40:2389
14. Doremus RH (1964) J Chem Phys 42:414
15. Smithard MA (1973) Sol State Commun 13:153
16. Sukumar V, Doremus RH (1993) Phys Stat Sol B 179:307
17. Nakao S, Saitoh K, Ikeyama M, Niwa H, Tanemura S, Miyagawa Y, Miyagawa S, Tazawa M, Jin P (1998) Nucl Instr Meth Phys Res B 141:246
18. Battaglin G, Cattaruzza E, D'Acapito F,Gonella F, Mazzoldi P, Mobilio S, Priolo F (1998) Nucl Instr Meth Phys Res B 141:252
19. Magruder RH, Zuhr RA (1998) Nucl Instr Meth Phys Res 141:256
20. White CW, Zhou DS, Zuhr RA, Magruder RH (1994) Trans Mater Res Soc Jpn 17:553
21. Williams EK, Ila D, Darwish A, Poker DB, Sarkisov SS, Curley MJ, Wang JC, Svetchnikov VL, Zandbergen HW (1999) Nucl Instr Meth Phys Res B 148:1074
22. Magruder RH, Yang L, Haglund RF, White CW, Yang L, Dorsinville R, Alfano RR (1993) Appl Phys Lett 62:1730
23. White CW, Zhou DS, Budai JD, Zuhr RA, Magruder RH, Osborne DH (1994) In: Culbertson RJ, Holland OW, Jones KS, Maex K (eds) Materials Synthesis and Processing Using Ion Beams Mat Res Soc Symp Proc Vol 316. Materials Research Society, Pittsburgh, PA, p 499
24. Henderson DO, Mu R, Ueda A, Tung YS, White CW, Zuhr RA, Zhu JG (1996) J Non-Cryst Sol 205–207:788
25. Honda S, Modine FA, Meldrum A, Budai JD, Haynes TE, Boatner LA, Gea LA (1999) In: Ewing RC, Lucas G, Williams JS, Zinkle SJ (eds) Microstructural processes in irradiated materials. Mat Res Soc Symp Proc Vol 540. Materials Research Society, Pittsburgh, PA, p 225
26. Alves E, da Silva RC, Conde O, da Silva MF, Soares JC (1999) Nucl Instr Meth Phys Res B 148:1049
27. Johnson E, Johansen A, Sarholt L, Dahmen U (1999) Nucl Instr Meth Phys Res B 148:1034
28. Henderson DO, Wu M, Ueda A, Tang YS, Mu R, Chen J, Gu Z, Collins WE, White CW, Budai JD, Meldrum A, Zuhr RA, Zhu JG (1998) Nucl Instr Meth Phys Res B 141:284
29. Heinig K-H, Schmidt B, Markwitz A, Grötzschel R, Strobel M, Oswald S (1999) Nucl Instr Meth Phys Res B 148:969
30. Withrow SP, White CW, Meldrum A, Budai JD (1999) J Appl Phys 86:396
31. Shimizu-Iwayama T, Fujita K, Nakao S, Saitoh K, Fujita T, Itoh N (1994) J Appl Phys 75:7779
32. Min KS, Shcheglov KV, Tang CM, Atwater HA, Brongersma ML, Polman A (1996) Appl Phys Lett 68:2033
33. Mutti P, Ghislotti G, Bertoni S, Bonoldi L, Cerofolini GF, Meda L, Grilli E, Guzzi M (1995) Appl Phys Lett 66:851
34. Mu R, Henderson DO, Tung YS, Ueda A, Hall C, Collins WE, White CW, Zuhr RH, Zhu JG (1996) J Vac Sci Technol 14:1482
35. White CW, Budai JD, Zhu JG, Withrow SP, Zuhr RA, Hembree DM, Henderson DO, Ueda A, Tung YS, Mu R, Magruder RH (1996) J Appl Phys 79:1876
36. White CW, Budai JD, Zhu JG, Withrow SP, Aziz MJ (1996) Appl Phys Lett 68:2389
37. Bonafos C, Garrido B, López M, Romano-Rodriguez A, Gonzáles-Varona O, Pérez-Rodriguez A, Morante JR (1998) Appl Phys Lett 72:3488
38. Meldrum A, White CW, Boatner LA, Zuhr RA, Anderson IM, Sonder E, Henderson DO (1999) Nucl Instr Meth Phys Res B 148:957
39. White CW, Budai JD, Withrow SP, Zhu JG, Sonder E, Zuhr RA, Meldrum A, Hembree DM, Henderson DO, Prawer S (1998) Nucl Instr Meth Phys Res B141:228
40. White CW, Budai JD, Zhu JG, Withrow SP, Hembree DM, Henderson DO, Ueda A, Tung YS, Mu R (1996) In: Poker DB, Ila D, Cheng YT, Harriott LR, Sigmon TW (eds) Ion-solid interactions for materials modification and processing, Mat Res Soc Symp Proc Vol 396. Materials Research Society, Pittsburgh, PA, p 397
41. Ekimov A, Gurevich S, Kudriavtsev I, Lublinskaya O, Merkulov A, Osinskii A, Vatnik M, Gandais M, Wang Y (1995) J Cryst Growth 151:38
42. Gea LA, Budai JD, Boatner LA (1999) J Mater Res 14:2602
43. Gea LA, Boatner LA, Rankin J, Budai JD (1995) In: Jacobson DC, Luzzi DE, Heinz TF, Iwaki M (eds) Beam-solid interactions for materials synthesis and characterization, Mat Res Soc Symp Proc Vol 354. Materials Research Society, Pittaburgh, PA, p 269
44. White CW, Sonder E, Budai JD, Meldrum A, Zuhr RA, Withrow SP, Henderson DO (1999) In: Zinkle SJ, Lucas G, Ewing RC, Williams J (eds) Microstructural processes in irradiated materials. Mat Res Soc Symp Proc Vol 540. Materials Research Society, Pittaburgh, PA, p 219
45. Anderson TS, Magruder RH, Zuhr RA, Wittig JE (1996) J Elect Mater 25:27
46. Tadaki T, Murai Y, Koreeda A, Nakata Y, Hirotsu Y (1996) Mater Sci Eng A217/218:235
47. Lee EH, Maziasz PJ, Rowcliffe AF (1981) In: Holland JR, Mansur LK, Potter DI (eds) Phase stability during irradiation. TMS/AIME, New York, p 191
48. Vance ER, Anderson BW (1972) Mineral Mag 38:605
49. Vance ER (1974) Mineral Mag 39:709
50. Hosono H, Matsunami N, Kudo A, Ohtsuka T (1994) Appl Phys Lett 65:1632
51. Hosono H, Kawamura K, Kameshima Y, Kawazoe H (1997) J Appl Phys 82:4232
52. Caccavale F, De Marchi G, Gonella F, Mazzoldi P, Meneghini C, Quaranta A, Arnold GW, Battaglin G, Mattei G (1995) Nucl Instr Meth Phys Res B 96:382
53. De Marchi G, Gonella F, Mazzoldi P, Battaglin G, Knystautas EJ, Meneghini C (1994) J Non-Cryst Sol 179:228
54. Ila D, Williams EK, Smith CC, Poker DB, Hensley DK, Klatt C, Kalbitzer S (1999) Nucl Instr Meth Phys Res B 148:1012
55. Reynolds RW, Boatner LA, Finch CB, Châtellain A, Abraham MM (1972) J Chem Phys 56:5607
56. Boatner LA, Sales BC (1988) In: Lutze W, Ewing RC (eds) Radioactive waste forms for the future. Elsevier, Amsterdam, p 495
57. Wang LM (1998) Nucl Instr Meth Phys Rev B 141:312
58. Allen CW, Ryan EA (1997) In: Robertson IM, Was GS, Hobbs LW, Diaz de la Rubia T (eds) Microstructure evolution during irradiation, Mat Res Soc Symp Proc Vol 439. Materials Research Society, Pittsburgh, PA, p 277

59. McCaffrey JP, Sullivan BT, Fraser JW, Callahan DL (1996) Micron 27:407
60. Meldrum A, Zinkle SJ, Boatner LA, Ewing RC (1999) Phys Rev B 59:3981
61. Virk HS (1995) Radiat Eff Def Sol 133:87
62. Zinkle SJ, Kinoshita C (1997) J Nucl Mater 251:200
63. Meldrum A, Boatner LA, Ewing RC (1997) Phys Rev B 56:13805
64. Wang LM, Cameron M, Weber WJ, Crowley KD, Ewing RC (1994) In: Brown PW, Constantz B (eds) Hydroxyapatite and related materials. CRC Press, London, p 243
65. Wolf D, Okamoto PR, Yip S, Lutsko JF, Kluge M (1989) J Mater Res 5:286
66. Devanathan R, Lam NQ, Okamoto PR (1993) Phys Rev B 48:42
67. Wang SX (1997) Ion beam irradiation-induced amorphization: nano-scale glass formation by cascade quenching. Ph.D. dissertation, Univ. New Mexico
68. Meldrum A, Boatner LA, Ewing RC (1997) J Mater Res 12:1816
69. Budai JD, White CW, Withrow SP, Chisholm MF, Zhu J, Zuhr RA (1997) Nature 390:384
70. Ziegler JF (1996) TRIM Version 96.01. IBM-Research, Yorktown, NY
71. Qin LC, Hobbs LW, (1995) J Non-Cryst Sol 192&193:456
72. Fisher SB (1970) Radiat Eff 5:239
73. Mu R, Ueda A, Wu M, Henderson DO, Malone K, Mills G, Meldrum A (1999) Proc Electrochem Soc 19:439
74. Meldrum A, Zuhr RA, Sonder E, Budai JD, White CW, Boatner LA, Ewing RC, Henderson DO (1999) Appl Phys Lett 74:697
75. Naguib HM, Kelly R (1975) Radiat Eff 25:1
76. Allen CW, McCormick AW, Baldo PM, Rehn L (1999) In: Ewing RC, Lucas G, Williams JS, Zinkle SJ (eds) Microstructural processes in irradiated materials, Mat Res Soc Symp Proc Vol 540. Materials Research Society, Pittsburgh, PA, p 561
77. Lindner, JKN (unpublished data)
78. Zhu JG, White CW, Wallis DJ, Budai JD, Withrow SP (1996) In: Poker DB, Ila D, Cheng Y-T, Harriott LR, Sigmon TW (eds) Ion-solid interactions for materials modification and processing, Mat Res Soc Symp Proc Vol 396. Materials Research Society, Pittsburgh, PA, p 447–452
79. Meldrum A, Sonder E, Zuhr RA, Anderson IM, White CW, Boatner LA, Henderson DO (in press) J Mater Res
80. McNallan MJ, Debroy T (1991) Metallurgical Trans 22B:557
81. Rodriguez JA, Chaturvedi S, Kuhn M (1998) J Chem Phys 108:3064
82. Zinkle SJ, Lee EH (1990) Metallurgical Trans 21A:1037
83. Follstaedt DM (1993) Appl Phys Lett 62:1116
84. Wong-Leung J, Williams JS, Elliman RG, Nygren E, Eaglesham DJ, Jacobson DC, Poate JM (1995) Nucl Instr Meth. Phys Res B96:253
85. Wong-Leung J, Nygren E, and Williams JS (1995) Appl Phys Lett 67:416
86. Raineri V, Fallica PG, Percolla G, Battaglia A, Barbagallo M, Campisano SU (1995) J Appl Phys 78:3727
87. Wong-Leung J, Ascheron CE, Petravic M, Elliman RG, and Williams JS (1995) Appl Phys Lett 66:1231
88. Follstaedt DM, Myers SM, Petersen GA, Medernach JW (1996) J Electr Mater 25:151
89. Myers SM, Follstaedt DM (1996) J Appl Phys 79:1337